Study of the angular resolution of the IceCube 59 string detector using the shadowing of cosmic rays by the Moon

Hugo Stiebel

Master Thesis, 45hp

University of Wisconsin-Madison and Stockholm University

January 13, 2011

Abstract

The IceCube Neutrino Observatory is a Cherenkov detector at the South Pole. It is designed to study neutrinos of astrophysical origin.

IceCube is also sensitive to atmospheric muons created by cosmic rays. This down-going muon flux is the dominant background in the search for astrophysical neutrinos but it can also be used to study the performance of the detector. The Moon blocks some of the cosmic rays from reaching Earth. This creates a deficit of atmospheric muons in the direction of the Moon and this shadow can be used as an experimental verification of the absolute pointing accuracy and the angular resolution of the detector.

In a previous analysis, for the 40-string version of the IceCube detector, the statistical significance of the Moon shadow was determined to 8σ.

In this thesis the Moon shadow of the larger 59-string detector have been investigated. This version has been taken data from the end of May 2009 to the end of May 2010. Two different analysis of the Moon shadow have been made, where the statistical significance of the Moon shadow was determined to 12σ.

The shadow appears to be shifted by $\sim 0.1^\circ$ in right ascension. The magnetic field could be partially responsible for this but by using the results of other experiments it is deemed unlikely to be the only cause for the shift. The small shift could also be due to statistical fluctuations, or it could be a systematic pointing error.

Acknowledgement

The IceCube collaboration consists of a great set of people and I owe a lot of them my gratitude. I will list a few of them here.

First of all I would like to thank my supervisors, Albrecht Karle and Per-Olof Hulth, for making this thesis possible.

I've been working closest with Laura Gladstone and she has been of great importance for this work. She has always been very helpful and friendly and devoted a lot of time to my problems.

Marcos Santander has also been very involved in my work. He has been very supportive and encouraging.

I also need to thank the rest of the Moon group that includes David Boersma, Jan Blumenthal and Chad Finley. I've had very helpful discussions with David and Jan.

Mike Baker and Jon Dumm have always been very friendly and they have helped answering a lot of questions.

UW-Madison and the IceCube group took very good care of me during my stay. Kim Kreiger, Frances Culwell and Terri Wipperfurth made me feel very welcome. And I would like to thank the rest of the people of IceCube that made my stay rememberable.

Most importantly I'd like to thank my family for all their love and support.

Contents

Chapter 1

Introduction

This Master Thesis is based on 30 weeks of work at the University of Wisconsin-Madison. The work have been focused on the Moon shadow which is caused by the absorption of cosmic rays by the Moon.

An introduction to cosmic rays, neutrinos and the astronomical coordinate systems used is given in Chapter 1. Chapter 2 discusses the physics behind neutrino detection and briefly how the detector and event reconstruction works. The Moon shadow is also discussed here in more detail. The data and simulation are described and compared in Chapter 3. In Chapter 4 the two analyses and the result is presented.

1.1 Cosmic rays

The Earth's atmosphere is constantly bombarded by energetic particles called cosmic rays. When these particles strike a molecule of the atmosphere, they produce a very large number of secondary particles. When this ionizing radiation was first discovered the cosmic ray particles were thought to be rays and not single particles, thereby the name.

Cosmic rays have been observed with energies spanning 14 orders of magnitude from 10^6 eV to over 10^{20} eV. This very high energy can be compared to the Large Hadron Collider in Geneva where particles will be accelerated to 10^{12} eV (14 TeV), in the center of mass frame.

1.1.1 History of cosmic rays

After Henri Becquerel's discovery of radioactivity it was observed that charged electroscopes slowly discharge with time. And the rate of discharge of an electroscope increase in the presence of radioactive material. Initially it was thought that the ionizing radiation responsible for the slow discharge came from the decay of radioactive elements in the earth.

In the year 1911-1912, Victor Hess made a series of experiments to study the source of the background radiation. He measured the radiation levels at different altitudes with

electroscopes aboard a balloon. Surprisingly, he found that the radiation levels increased with altitude. Hess interpreted this result to mean that ionizing radiation is entering the atmosphere from outer space. Hess also ruled out the Sun as the radiation's source by making a balloon ascent during a near-total eclipse [1]. He gave this phenomenon the name "Cosmic Radiation", which later evolved to "Cosmic Rays". Hess was awarded the Nobel Prize in 1936 for his discovery of cosmic rays.

Cosmic rays have had a key role for the development of particle physics, before the man-made high-energy particle accelerators. The muon, the pion, the positron and particles containing the s quarks were first discovered in cosmic-ray induced reactions.

1.1.2 The cosmic ray energy spectrum

The cosmic ray energy spectrum follows a power law function, over several orders of magnitude, with a power index, α, close to 3:

$$\frac{dN}{dE} \propto E^{-\alpha} \tag{1.1}$$

The observed flux of cosmic rays is shown in Fig. 1.1. The steepening that occurs between 10^{15} and 10^{16} eV is known as the knee of the spectrum. This part of the spectrum is believed to be dominated by galactic sources (stars, supernovae). The onset of an extragalactic contribution could be signaled by the so-called second knee. The feature around 10^{19} eV is called the ankle of the spectrum. These ultra-high-energy cosmic rays are likely to be originating from extra galactic sources. One likely extra galactic source is an active galactic nucleus (AGN). A supermassive black hole is believed to be responsible for the energetic radiation produced in an AGN.

Much of the particles traveling towards Earth from cosmological distances do not make it all the way here:

- Optical photons can be obscured or diffused by dust, gas and background radiation. The galactic core of the Milky Way for example is completely obscured by dense gas.
- Cosmic rays that come in the form of high energy photons (gamma rays) can be absorbed by background light. This limits the range in which high energy gamma rays can travel. Above 1 PeV, only gamma rays from our own galaxy are visible.

$$\gamma + \gamma_{bkg} \rightarrow e^+ + e^-$$

- Charged particles are affected by magnetic fields that distorts their paths which makes it impossible to discern where they come from.
- Cosmic-ray protons with energies exceeding a threshold energy of $\sim 4 \cdot 10^{19}$ eV is predicted to interact with cosmic microwave background photons to produce pions.

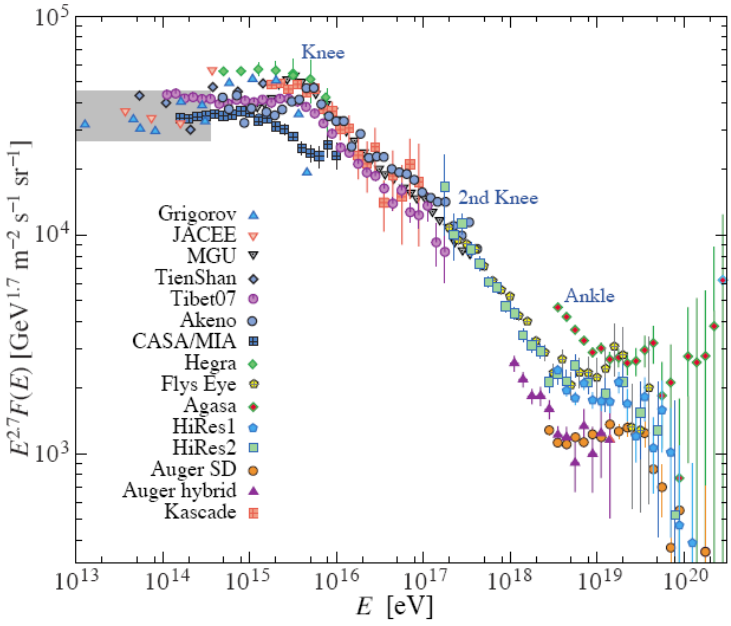

Fig. 1.1: The high-energy cosmic-ray spectrum follows a sequence of 3 power laws, separated by the knee and the ankle. The GZK cut-off limits the maximum energy of the flux. The flux is multiplied by $E^{2.7}$ to enhance the spectral features, from [2].

This is known as the Greisen-Zatsepin-Kuzmin limit (GZK limit).

$$p + \gamma_{bkg} \rightarrow \Delta^{+} \rightarrow p + \pi^{0}$$

$$p + \gamma_{bkg} \rightarrow \Delta^{+} \rightarrow n + \pi^{+}$$

Neutrinos are not affected by the process described above and can travel great distances with very little attenuation.

1.1.3 Cosmic ray air showers

When a primary cosmic ray (i.e. one of extraterrestrial origin) enters the atmosphere and strikes a molecule in the air, many high energy particles (secondaries) is produced. These secondary particles in turn create more secondaries, and so on, -in the end you get a-shower of particles. The particles produced in such collisions are typically mesons (e.g. pions and kaons) which mainly decay into photons or muons and neutrinos.

$$\pi^{0} \rightarrow \gamma + \gamma \tag{1.2}$$

$$\pi^+ \rightarrow \mu^+ + \nu_\mu \tag{1.3}$$

$$\pi^- \rightarrow \mu^- + \bar{\nu}_\mu \tag{1.4}$$

The muons continue in the original track of the primary cosmic ray within about one degree of the primary particle's path. Millions of particles can be created in an air shower

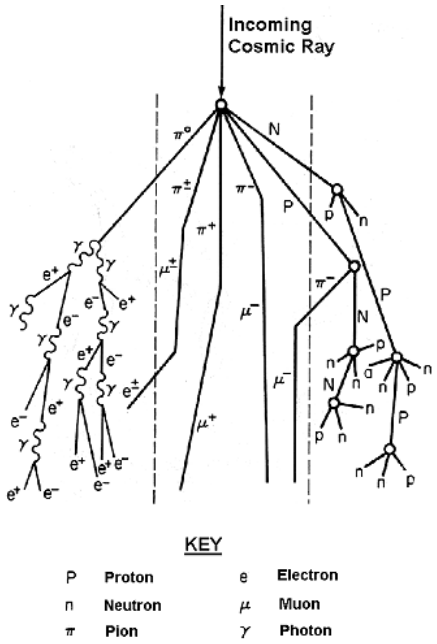

Fig. 1.2: An incoming cosmic ray strikes a particle in the atmosphere and initiates an air shower. The muons created in the shower are particularly important for this work. Note that the neutrinos produced in the cascade is not shown in the figure.

1.2 Neutrinos

The three charged leptons: e, μ, and τ all have a neutral counterpart; the electron neutrino ν_e, the muon neutrino ν_μ and the tau neutrino ν_τ. Neutrinos are, like the rest of the leptons, fermions (spin-$\frac{1}{2}$ particles).

In the Standard Model neutrinos are massless but several experiments indicates that neutrinos oscillates between their different weak-interaction eigenstates, ν_e, ν_μ, ν_τ. If neutrinos oscillate they cannot travel at the speed of light[1] and therefore they must have

[1]Time stand still for a particle traveling at the speed of light.

a nonzero mass.

Apart from their possible gravitational interactions, neutrinos only interact, with matter through the weak force. The cross section for neutrino interactions with matter is therefore very small. Since neutrinos are neither deflected by magnetic fields nor significantly attenuated by matter and radiation they provide an undistorted view of the high energy universe. Because of this neutrinos are also very difficult to detect. Immense particle detectors are required to collect cosmic neutrinos in statistically significant numbers.

It is not well understood how or where the energetic cosmic ray particles are accelerated. But in the energetic environments in which high energy cosmic rays are accelerated there are likely to exist matter or radiation fields, which the accelerated hadrons can interact with, to produce pions or kaons [2].

The neutral pions that are produced decay to gamma rays (Eq. 1.2). Charged pions decay to neutrinos:

$$\pi^+ \rightarrow \mu^+ + \nu_\mu \rightarrow e^+ + \nu_\mu + \nu_e + \bar{\nu}_\mu \tag{1.5}$$

$$\pi^- \rightarrow \mu^- + \bar{\nu}_\mu \rightarrow e^- + \nu_\mu + \bar{\nu}_e + \bar{\nu}_\mu \tag{1.6}$$

1.3 Coordinate systems

The Earth is constantly moving through space; it is rotating around its own axis and around the Sun. The rotation axis also has a slow wobble. This results in the constantly changing positions of celestial objects as viewed from Earth. In astronomy there are therefore several coordinate systems that are used to describe the positions of astronomical objects. These coordinate systems are called celestial coordinate systems and maps positions on the celestial sphere, which is an imaginary sphere of arbitrarily large radius, with the Earth located at its center.

Celestial coordinate systems use a system of spherical coordinates projected on the celestial sphere, in analogy to the geographic coordinate system used on the surface of the Earth. The two most common coordinate systems is the horizontal and the equatorial coordinate systems.

1.3.1 The horizontal coordinate system

The horizontal coordinate system is based on a fixed position on the Earth's surface, which revolves around Earth's rotation axis once every 23.9 hours. This makes the coordinates of a fixed point on the celestial sphere to change as the Earth rotates.

The coordinates for the horizontal coordinate system is measured in Azimuth and Zenith. Azimuth ranges from 0° to 360° around the horizon of Earth. Zenith ranges from 0 t o 180°. The Zenith angle is 0° when looking straight up, the horizon has the value 90° and straight down to Earth's center 180°.

The term, local coordinates, can also be used to refer to horizon coordinates.

1.3.2 The equatorial coordinate system

The equatorial coordinate system is centered at Earth's center and fixes the sky around it, so that the sky appears fixed while we on the surface move as the planet turns. The equatorial coordinates of a celestial object is nearly constant in time. The two angles in an equatorial coordinate system is called right ascension (RA or α) and declination (Dec or δ).

Right ascension ranges from 0° to 360° and declination from $\pm 90^\circ$. Objects in the northern celestial hemisphere have a positive declination, and those in the southern celestial hemisphere have a negative declination.

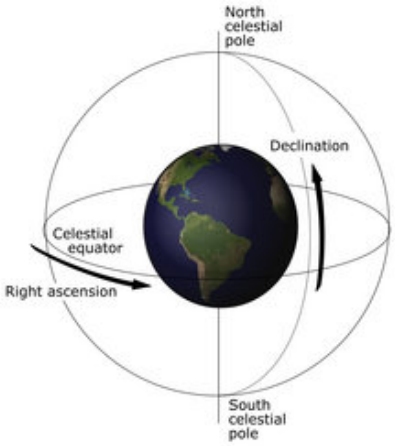

Fig. 1.3: The equatorial coordinate system; A point on the celestial sphere is described by the parameters; Right Ascension (RA or α) and Declination (Dec or δ).

Chapter 2

The IceCube Neutrino Telescope

IceCube is a Cherenkov detector designed to detect high energy astrophysical neutrinos. It is located at the geographic South Pole where it uses the clear Antarctic ice as detector material. Optical sensors in the ice can detect the Cherenkov light that is emitted by energetic particles going through the ice.

The final version of IceCube will consist of 80 strings (+6 DeepCore strings) with 60 optical sensors. The Data used in this analysis is taken by the 59-sting configuration of IceCube, we will refer to it as IC59.

2.1 Neutrino detection and telescopes

Neutrinos can interact with matter in two ways; via the neutral current (involving the exchange of a Z boson) or charged current (involving the exchange of a W boson) [3].

The annihilation reaction:

$$e^+ + e^- \rightarrow \nu_\mu + \bar{\nu}_\mu \tag{2.1}$$

and the elastic scattering reaction:

$$\nu_\mu + e^- \rightarrow \nu_\mu + e^+ \tag{2.2}$$

involves the exchange of the neutral Z boson.

In a charged current interaction, the neutrino transforms into its partner lepton (electron, muon, or tau). Since this interaction involves the exchange of a charged boson, the target particle also changes character (e.g., a neutron transforms into a proton). For example in the reaction:

$$\nu_e + {}^{71}Ga \rightarrow {}^{71}Ge + e^- \tag{2.3}$$

the charged W boson is exchanged and gallium is transformed into germanium.

The cross-section for a neutrino interaction is very small. This is because the Z and W bosons are massive particles (more than 80 times heavier that the proton). Their large mass is the reason why weak interactions are heavily suppressed at low energies. Because of the small cross-section for a neutrino interaction neutrino detectors must be very large in order to detect a significant number of neutrinos.

There are various detection methods that have been used to study neutrinos.

One type of neutrino detectors uses a tank containing the target material. A neutrino interacting via the charge current transforms a target atom into a new element. The number of transformed atoms is then a measure of the neutrino flux. The SAGE and GALLEX neutrino detectors are two such detectors. The target material is gallium which is transformed into germanium, see Eq. 2.3.

Cherenkov detectors are another type of detectors that can detect neutrinos. In these detectors, a large volume of clear material (e.g., water or ice) is surrounded by optical sensors. A neutrino with sufficient energy can produce charged leptons (Eq. 2.2 - 2.3) that travels faster than the speed of light in the detector medium. These particles emit Cherenkov light that can be detected by the optical sensors.

Deep underground in Kamioka, Japan, a set of groundbreaking neutrino experiments have taken place, using a large water tank fitted with thousands of optical sensors. The detector is sensitive to neutrinos from the Sun that can be detected from the elastic scattering process described above in Eq. 2.2. The recoiling electrons emit Cherenkov light which is detectable with the optical sensors.

The Antarctic Impulse Transient Antenna (ANITA) is a balloon-born device flying over Antarctica. It is sensitive to the Askaryan radiation produced by high-energy ($\sim 10^{18}$ eV) neutrinos interacting with the ice below.

The Askaryan effect is similar to the Cherenkov effect. A high-energy particle traveling in a dense dielectric material produces showers of secondary charged particles. Scattering processes and positron annihilation lead to a $\sim$20% negative charge asymmetry in the electron-photon part of the shower, this charge asymmetry creates a cone of coherent radiation in the radio or microwave part of the electromagnetic spectrum.

The Sun is the dominant source of neutrinos and several experiments have measured the neutrino flux from the Sun, e.g. GALLEX, SAGE and Kamikoande as described above. The discovery of the neutrino oscillation was made by studying these solar neutrinos.

In 1987 a supernova was spotted in the Large Magellanic Cloud. Neutrinos from this famous supernova (SN1987A) were detected in the two water Cherenkov detectors; Irvine Michigan Brookhaven and Kamikoande. Since the detection of the supernova 1987A many new detectors have been designed to function as neutrino telescopes.

The two observations of solar and supernova neutrinos have been of great importance. The former showed that neutrinos have a tiny mass, opening the first crack in the Standard Model of Particle Physics, and the latter confirmed the theory of stellar evolution as well

as the basic nuclear physics of the death of stars.

The advantages for using the neutrino as an astronomical messenger will probably result in more important discoveries.

2.1.1 Muon energy loss

Generally, as a muon travels through matter, it loses energy due to ionization losses, bremsstrahlung, pair production and photo-nuclear interaction.

When a muon ionize an atom by knocking out an electron it losses energy. The energy loss through ionization is described by the Bethe-Bloch formula.

Bremsstrahlung is photons produced when a muon interacts with the electromagnetic field of atomic nuclei. Pair production is e^+e^- pairs that are produced as a muon pass through a material. A muon can also interact with a nucleon to produce a cascade of secondary particles, this is called a photonuclear interaction.

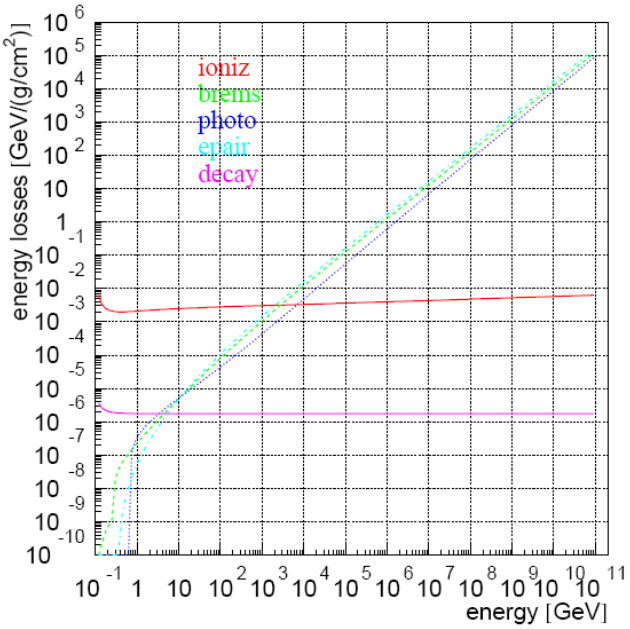

Fig. 2.1: Muon energy loss in ice, from [4]

At low energy the ionization energy loss dominates. At higher energy Bremssthralung, Pair-production and Photonuclear processes are the dominating factors. Ionization occurs continuously, while the three others are stochastic, energy-dependent processes. The average rate of muon energy loss is given by:

$$-\frac{dE}{dx} = a + bE \tag{2.4}$$

where E is the energy of the muon, a is the constant ionization energy loss and b the sum of the stochastic energy losses.

The critical energy, ϵ, is the energy where the factor bE starts to dominate the average rate of muon loss.

$$\epsilon = \frac{a}{b} \tag{2.5}$$

with a = 0.212/1.2 $\frac{GeV}{mwe}$ and b = $0.251 \cdot 10^{-3}/1.2$ $\frac{1}{mwe}$ (mwe = meters of water equivalent), from [4]. For muons in ice ϵ = 845 GeV.

The average energy, E, for a muon with the initial energy, E_0, can be expressed by [5]:

$$E = (E_0 + \epsilon)e^{-bx} - \epsilon \tag{2.6}$$

after propagating a distance, x. A muon with an initial energy of 3 TeV have in average an energy of 2 TeV after passing through 1500 meters of ice.

High-energy muons also emit Cherenkov radiation (see next section) but this process is not an important energy loss.

2.1.2 Cherenkov radiation

When an electrically charged particle passes through a dielectric medium it polarizes the molecules of the medium. Photons will be emitted as the electrons restore themselves to equilibrium after the charge has passed. In normal circumstances, these photons destructively interfere with each other. If the particle travels faster than the speed of light in the medium, the photons will constructively interfere and intensify the observed radiation. An electromagnetic shock-wave is created along the path: that is, a coherent wave-front of radiation similar to the more familiar effect of a sonic boom from a supersonic aircraft. The phenomenon is called the Cherenkov effect and the light that is emitted is called Cherenkov radiation.

In figure 2.2 the Cherenkov effect is illustrated. A particle is traveling horizontally with a speed v_p. We let β be the ratio between the speed of the particle, v_p, and the speed of light, c, ($\beta = v_p/\mathrm{c}$). After a time t the particle has traveled a distance of:

$$x_1 = v_p t = \beta c t \tag{2.7}$$

The emitted light waves (blue circles) travel at speed the speed of light in the medium, c/n. After a time t the light has traveled a distance of:

$$x_2 = \frac{c}{n} t \tag{2.8}$$

Solving for the angle θ in the right angle triangle:

$$cos\theta = \frac{x_2}{x_1} = \frac{1}{n\beta} \tag{2.9}$$

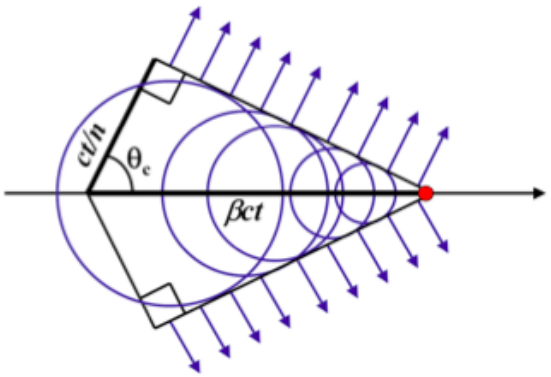

Fig. 2.2: The Cherenkov effect; a charged particle, traveling with a speed $\beta c > \frac{c}{n}$, creates a shockfront. The Cherenkov angle, θ, is given by Eq. 2.9.

For water, with a refractive index n = 1.33, the Cherenkov angle is about 41°. A particle's track can be deduced from the Cherenkov cone, making this effect very useful for building telescopes.

2.2 Detector overview

IceCube is a Cherenkov detector at the geographic South Pole. It consists of digital photomultipliers (DOMs) that are sensitive to Cherenkov light. The DOMs are attached to strings that have been lowered down in drilled deep holes in the ice. There are sixty DOMs on each string.

The construction of IceCube began in 2005, when the first string of DOMs was deployed. Each summer (Antarctic summer) since then more strings have been deployed and construction will be completed during the 2010-2011 season. When completed the detector consists of 80 strings, each with 60 DOMs at depths ranging from 1,450 to 2,450 meters.

Each string is associated with an IceTop station, comprised of two tanks, each with two DOMs. IceTop is used as a cosmic ray air-shower detector, for cosmic ray composition studies. IceTop can also be used to veto air-showers in IceCube.

Deepcore is another part of the detector that is optimized for low energy events, ideal for dark matter WIMP searches. It consists of 6 strings and it is a more compact Cherenkov detector located in the clear ice of the bottom center of the detector.

Fig. 2.3 shows the design of IceCube, IceTop, Deepcore and the Amanda detector which is the predecessor to IceCube.

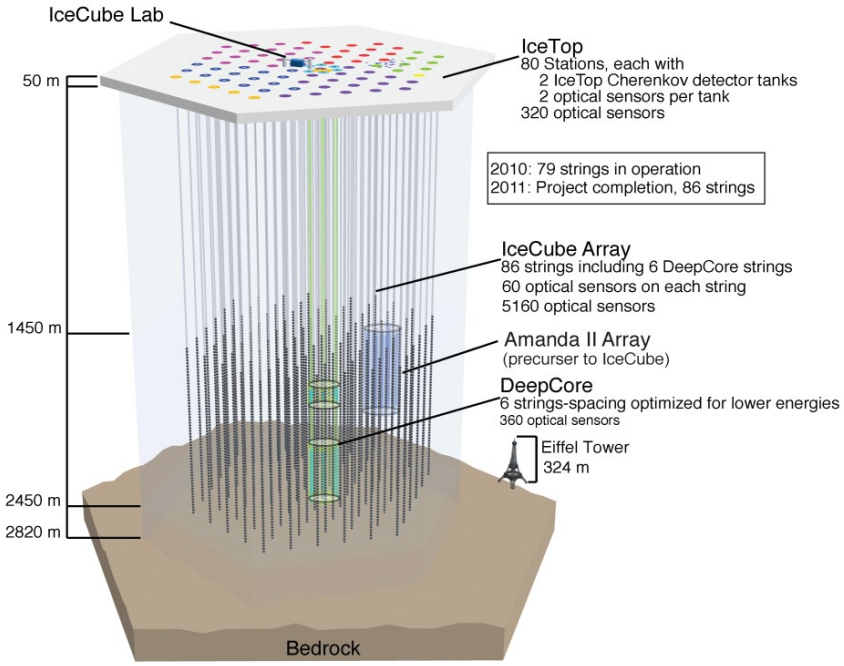

Fig. 2.3: The design of the IceCube neutrino detector with 5,160 optical sensors arranged on strings deep down in the clear Antarctic ice. The signals detected by each sensor are transmitted to the surface over the 86 cables to which the sensors are attached. IceCube encloses it's smaller predecessor, AMANDA.

2.3 Event reconstruction

An air shower initiated by cosmic rays consists of bundles of muons, the muons that survive all the way to the detector can be detected by the Cherenkov light they emit when they go through the detector. This is register as a down-going event. Fig. 2.4 shows a down-going event. The circles represent DOMs that have registered light, the size of the circles shows

the number of detected photons. The color represent the time, from red (earliest) to blue (latest). The line is the direction of the muon track. The events in this analysis are all down-going events.

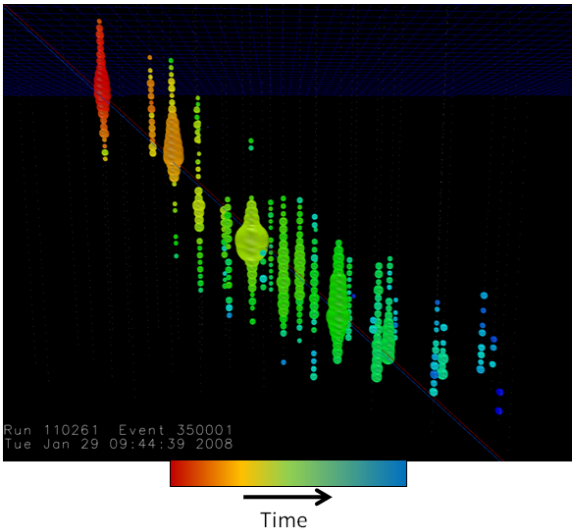

Fig. 2.4: A down going event in the 40-string IceCube detector. Each circle represents one active optical module; the size of the circles shows the number of detected photons, while the color represents the time, from red (earliest) to blue (latest).

Events are reconstructed using maximum likelihood methods. The likelihood fits are seeded with a first guess to find the starting point. For muons, the main first guess is to fit a plane wave to the detection times in the DOMs. For a muon, the plane wave should have a velocity very close to the speed of light. The maximum likelihood fitter then calculates the likelihood for different track positions and directions. It does this by using functions which account for the light propagation through the ice. The likelihood reconstruction used in this analysis is called SPE (Single Photo-Electron).

The event variable Rlogl is the reduced log-likelihood of the track reconstruction fit. The term "reduced" means that the logarithm of the likelihood has been normalized by dividing it by the number of degrees of freedom (NDF) in the track fit, which usually is the number of hit DOMs, minus the number of fitted parameters (five in the track fits):

$$\text{Rlogl} = \frac{\log \mathcal{L}}{\text{NDF}} = \frac{\log \mathcal{L}}{N_{\text{ch}} - N_{\text{par}}} = \frac{\log \mathcal{L}}{N_{\text{ch}} - 5} \tag{2.10}$$

The Paraboloid method uses the likelihood reconstruction to estimate the angular resolution of the reconstructed track. Paraboloid evaluates the likelihood function in the neighborhood of the best fit, and constructs a best-fit parabola to the shape of the likelihood. An example is illustrated in Fig. 2.5. The minimum of this parabola is used as Paraboloid's best estimate of the track direction, and the width of the parabola provides an estimate of the uncertainty. Fig. 2.11 shows the error ellipse (the width of the parabola) that Paraboloid generates.

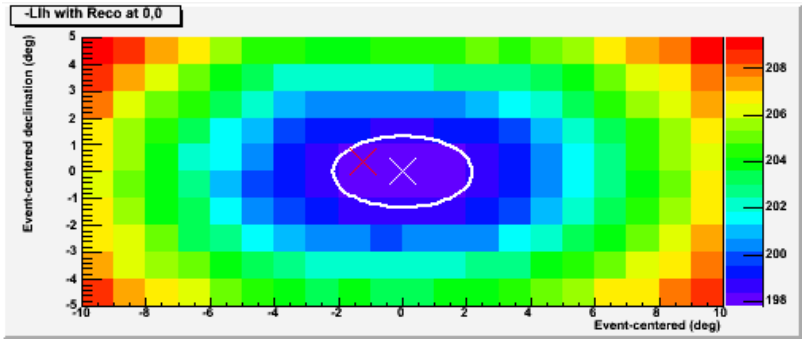

Fig. 2.5: This figure shows the likelihood function of a simulated event. A paraboloid is fitted to the most likely position. The white X-mark is the reconstructed direction of the event and the the red X-mark is the true direction. The white ellipse is the error ellipse in Fig. 2.11.

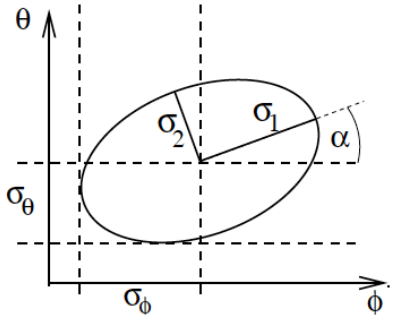

Fig. 2.6: The Paraboloid method generates an error ellipse for each event. The major and minor axes σ_1 and σ_2, of the ellipse represent the angular uncertainty. The picture is taken from [7].

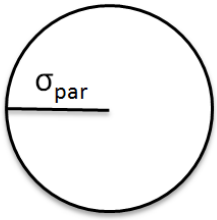

Fig. 2.7: The RMS value of the ellipse in Fig. 2.11 represents a circle. The RMS value will be referred to as the Paraboloid sigma, σ_{par}.

The Root Mean Square (RMS) of the two errors that the Paraboloid method generates

is used in this analysis. We call it the Paraboloid sigma, σ_{par}, and it is a measure of the reconstruction quality.

$$\sigma_{par} = \sqrt{\frac{\sigma_1^2 + \sigma_2^2}{2}} \tag{2.11}$$

MuE is an energy estimator of a muon track. It derives the energy by calculating the average number of photons emitted per unit length of a muon track. It takes into account the absorptions and scattering of light in the ice, the quantum efficiency of the DOMs and the geometries of the reconstructed track and the DOMs.

2.4 Angular resolution

The Point Spread Function (PSF) of a telescope describes how the image of a point source is distorted. A good resolution and pointing accuracy is important for resolving possible neutrino point sources.

The experimental determination of the PSF and the pointing accuracy for an optical telescope is often very straightforward due to the ample supply of point sources. For a neutrino telescopes this becomes trickier. Instead of using a point source it is common for a cosmic ray detector to use the Moon shadow for calibrations.

2.4.1 Moon shadow

As the Moon moves over the sky it blocks some of the cosmic rays from reaching Earth. From the direction of the Moon there is therefore a small deficit of atmospheric muons. The idea of a Moon shadow was first proposed in 1957 [6], and has become an established observation for a number of astroparticle physics experiments.

The Moon has an 18.6 year cycle, under which the maximum position over the horizon that the Moon reaches varies (Fig. 2.9). This analysis have used data taken by IC59 (the 59-string detector), from June 2009 to June 2010. The highest position in the sky for the Moon in this data set was -26° in declination.

2.4.2 Magnetic deflection

In the TeV regime, the paths of charged Cosmic rays are noticeably bent by the magnetic fields of Earth. This results in an offset of the Moon shadow from the nominal positions, see Fig. 2.10. The amount of deflection depends on the charge and energy of the primary particle, as well as the magnitude and direction of the magnetic field.

Tibet-III and ARGO-YBJ are two cosmic ray detectors located in Tibet, China [8][9]. These detectors have studied the Moon shadow with very high statistics. Fig. 2.11 shows a plot of the displacement of the Moon shadow caused by the geomagnetic field as seen by the Tibet-III experiment. The energies of the primary cosmic rays are deduced from the

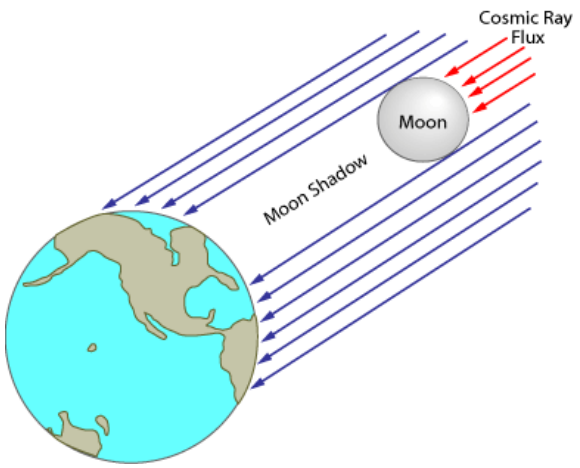

Fig. 2.8: The Moon blocks some of the cosmic ray flux. This creates a shadow of the Moon caused by the cosmic ray flux.

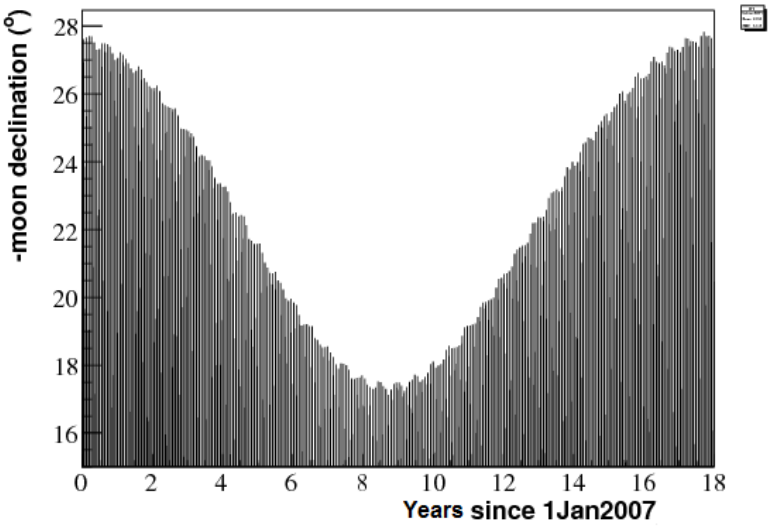

Fig. 2.9: The maximum declination of the Moon at the South Pole varies over an 18.6 year cycle. The data used in this analysis was taken in 2009-2010. The maximum declination for this period was -26°

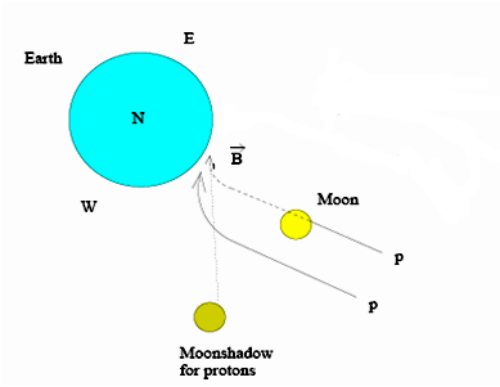

Fig. 2.10: Positively charged particles are deflected by Earth's magnetic field in the East-ward direction. This result in a shift of the Moon shadow in the Westward direction.

air shower size (the shower size depends on the energy of the primary cosmic ray). The parameter $\Sigma\rho$ FT in the figure is the sum of the number of particles per m^2.

The energies of the primary cosmic rays are higher for the IceCube detector and thus the displacement of the Moon shadow should be much less (will be discussed in Chapter 3).

The relation between the displacement in right ascension, $\Delta\alpha$, the energy, E (in TeV), and the number of protons, Z, of the cosmic ray is expressed by the formula:

$$\Delta\alpha \approx \frac{1.6^\circ \cdot Z}{E(TeV)} \tag{2.12}$$

The cosmic rays all have different energy and those with lower energy are deflected more. This result in a shadow that looks "smeared-out" in the West-ward direction.

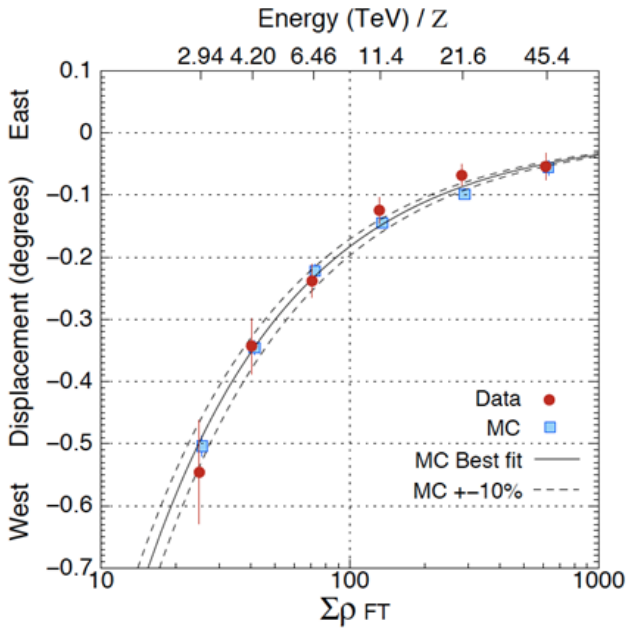

Fig. 2.11: The displacement of the Moons shadow in the east-west direction depends on the energy of the primary cosmic ray. The energy is measured with $\Sigma\rho$ FT which is a measure of the air shower size. The filled circles show the experimental data and open squares represent the MC (Monte Carlo) simulation. The solid curve is fitted to the MC events, and the dashed curves show a $\pm 10\%$ deviation from the solid curve. This is results from the Tibet-III experiment [9].

Chapter 3

Data and Simulation

3.1 Data

Data transfer from the South Pole is limited by the bandwidth of two satellites; thus, not all data from the detector can be transmitted. The data used for the study of the Moon shadow have passed a special filter on the South Pole to reduce the data transfer. Only events with a minimum quality and a reconstructed direction within a window around the direction of the Moon are selected by the Moon filter. The reconstruction used for the online event selection is a single (i.e. not iterated) log-likelihood fit.

The Moon filter is defined as follows:

- The Moon must be at least 15° above the horizon
- At least 12 DOMs must register each event
- At least 3 strings must contain hit DOMs
- The reconstructed direction must be within 10° of the Moon in declination.
- The reconstructed direction must be within 40° / $\cos(\delta)$ of the Moon in right ascension; the $\cos(\delta)$ factor corrects for projection effects.

When the data from the South Pole arrive to the northern hemisphere, more computation heavy reconstructions are done.

A typical month of data that is shown in Fig. 3.1. The event rates near the Moon increase as the Moon rises above the horizon. This is because of the strong increase in the muon flux with increasing zenith angle. This creates the dominant shape in the figure. The atmospheric muon flux depends on the zenith angle because the more atmosphere and ice the muons have to pass the more they get attenuated.

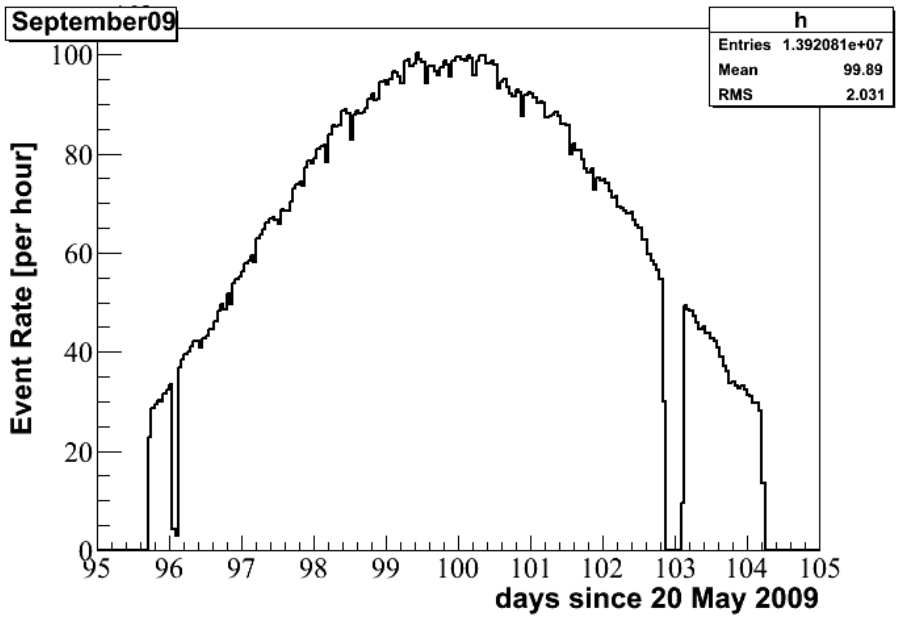

Fig. 3.1: An event rate plot for the month of September, data is taken over a period of 7-8 days when the Moon is more than 15° above the horizon. The event rate increase as the Moon rises in the sky, until the Moon reaches its highest position. When the Moon then goes down the count rate decreases. The data sample from this Moon cycle consists of 14 million events, which have passed the Moon filter. IC59 started registering data the 20th of May 2009.

3.2 Simulation

The detection process; from the initiation of the air shower by the primary particle to the detection of muons in the detector, was simulated using Monte-Carlo (MC) software.

The cosmic ray air showers were simulated using the software package CORSIKA (COsmic Ray SImulations for KAscade). The propagation of particles through the ice and the detector's response was simulated using other MC techniques. The resulting events were then reconstructed just like the real data, as described in Chapter 2.

The simulated data sample used for this analysis consist of two million events.

The two plots, Fig. 3.2 and Fig. 3.3, compare the distributions of the simulated data and the real (detector) data. Fig. 3.2 is a comparison of the reconstructed declination of real and simulated events. The error bars for the black curve (real data) is much smaller because of the higher statistics of the data sample. Fig. 3.3 shows the reconstructed energy of simulated and real events. The energy was estimated using the MuE-energy

reconstruction.

The distributions of the energies of the primary cosmic ray, the muon in the ice and the reconstructed energy is shown in Fig. 3.4. The median primary energy is 38.6 TeV and the median reconstructed muon energy is 1.8 TeV.

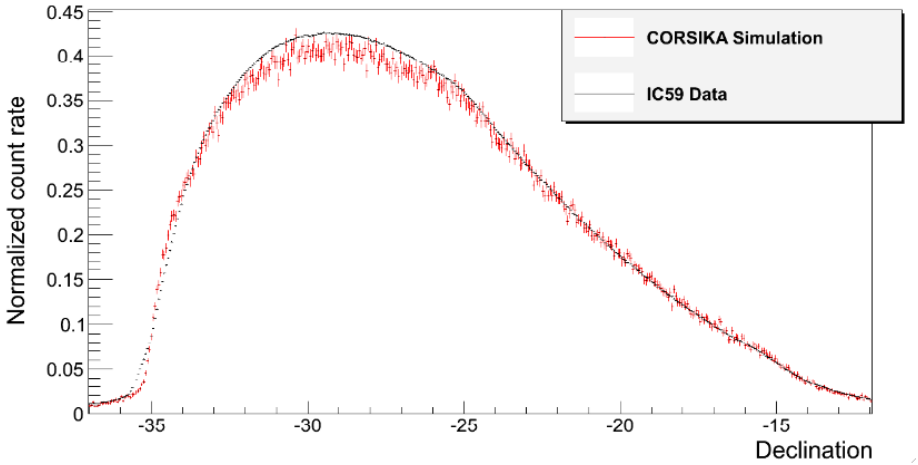

Fig. 3.2: Distribution of the reconstructed declination of real events, black curve, and simulated events, red curve. The error bars for the data (black curve) is much smaller because of the high statistics of the data sample.

If we assume that the deflection that the cosmic rays experience is the same for particles traveling towards Tibet as for particles travelling towards the South Pole then we can estimate the shift of the Moon shadow caused by the geomagnetic field using the results from the Tibet and the ARGO experiments. The cosmic ray energy in Fig. 3.4 is put into Eq. 2.12 to calculate the distribution of the displacement angle. The result is a median displacement of 0.05° and the distribution can be seen in Fig. 3.5.

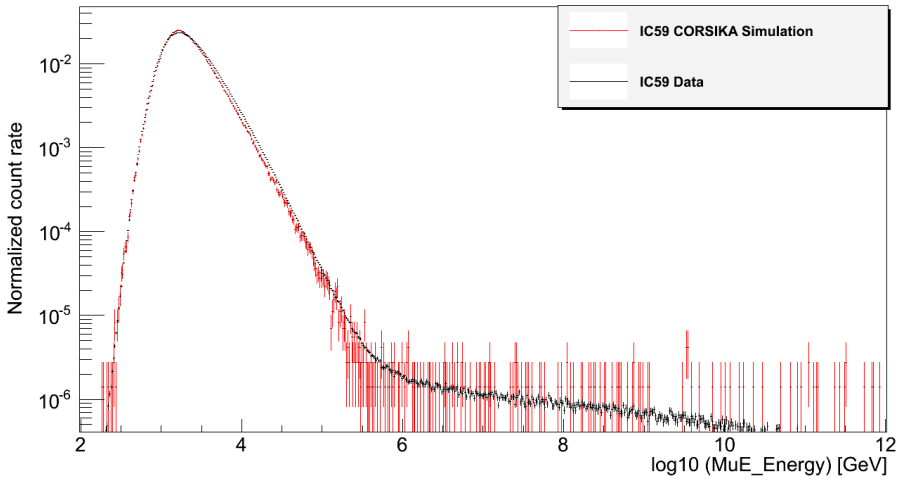

Fig. 3.3: Energy comparison between the reconstructed energy of the MC data and the real data. The energy reconstruction sometimes fail and this can result in a reconstructed energy that is too high.

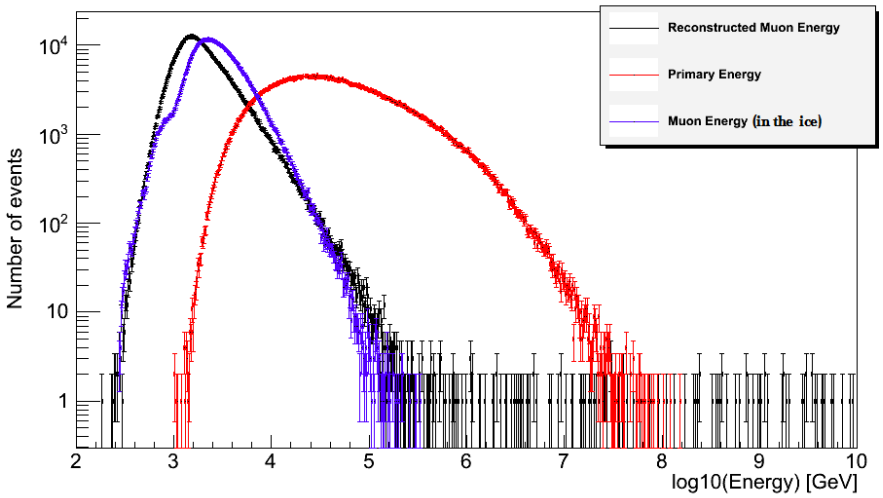

Fig. 3.4: The energy distribution of the simulated data set. The red curve is the primary energy of the cosmic ray, the median primary energy is 38.6 TeV. The blue curve represent the muon energy outside the detector in the Antarctic ice, the median muon energy is 2.6 TeV. The black curve is the reconstructed muon energy, the median reconstructed energy is 1.8 TeV (the energy reconstruction sometimes fail and this can result in an energy that is too high).

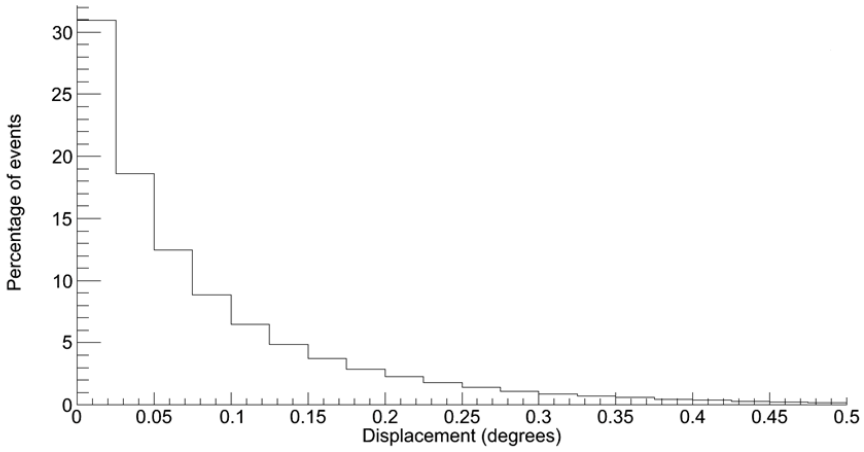

Fig. 3.5: The deflection angle of the cosmic ray is calculated using the energy distribution of the primary cosmic ray energy in Fig. 3.4 and the results of the Tibet-III and ARGO-YBJ experiments, Eq. 2.12. The median displacement angle in the histogram is 0.05°.

Chapter 4

Analysis

Two different methods have been used to study the Moon shadow. The method described in the next section, have successfully been applied to data from the 40-string configuration of IceCube. The significance of the Moon deficit was 8σ for a year of data taken by the 40-string configuration. We will call this method for the Binned method. The events are counted in bins that are larger than the size of the Moon.

The other method uses bins that are much smaller than the Moon. We will refer to the second method as the fine binned method.

4.1 Binned analysis

As the Moon moves over the sky the equatorial coordinates (α,δ) that are usually used for astronomical objects constantly change. To be able to see the Moon shadow it is necessary to use Moon centered coordinates. The events are centered around the Moon by subtracting the Moon's coordinates from the event's coordinates.

The declination coordinate becomes: $\Delta\delta = \delta_{Event} - \delta_{Moon}$ and the right ascension coordinate becomes: $\Delta\alpha = (\alpha_{Event} - \alpha_{Moon}) \cdot cos(\delta_{Moon})$. The cos($\delta$) factor is used to map equal areas of the sky on a two dimensional grid.

4.1.1 Cut values

There are a several quality parameters that give information of how well an event has been reconstructed. We want to cut out the events of low quality to maximize the significance. When we cut on the data we also lose information. There is a trade-off between reducing low quality events and keeping a larger data sample for statistics.

The cuts have been determined using the 2 Million Monte Carlo events, see Chapter 3.

The statistical significance of a signal is proportional to the number of signal events, N_{sig} (in this case a lack of events), over the square root of the background events, N_{bkgd}:

$$significance \sim \frac{N_{sig}}{\sqrt{N_{bkgd}}} \tag{4.1}$$

The signal, N_{sig}, is proportional to the fraction of events passing the cut, i.e. the efficiency, η:

$$N_{sig} \propto \eta \tag{4.2}$$

The background, N_{bkgd}, is proportional to the area of a bin and the efficiency η.

$$N_{bkgd} \propto \eta \cdot Area = \eta \cdot \pi r^2 \quad \rightarrow \quad \sqrt{N_{bkgd}} \propto \sqrt{\eta} \cdot r \tag{4.3}$$

Using the above equations we get a relation between the significance and the cut efficiency.

$$significance \sim \frac{N_{sig}}{\sqrt{N_{bkgd}}} \propto \frac{\eta}{\sqrt{\eta} \cdot r} = \frac{\sqrt{\eta}}{r} \tag{4.4}$$

The optimal bin radius should be equal to the median angular resolution, Ψ_{med}. Ψ is given from the simulation as the angular difference between the direction of the primary cosmic ray and the reconstructed track. By setting $r = \Psi_{med}$ in Eq. 4.4 we get:

$$significance \propto \frac{\sqrt{\eta(cuts)}}{\Delta\Psi_{med}(cuts)} \tag{4.5}$$

where the value of η and Ψ_{med} change for different cuts on the data.

The quality parameters used in this study are the Paraboloid sigma, σ_{para}, and the Rlogl parameter, as defined in Chapter 2. Eq. 4.5 is plotted in a two-dimensional histogram for different cuts on Rlogl and σ_{para}.

These quality cuts are chosen (see Fig. 4.1):

- Paraboloid sigma, $\sigma_{para} < 1.04$
- Rlogl < 8.8

The total number of events in the Moon sample is 170 million events. After the cuts 61 million events remain. 65% of the events is cut out.

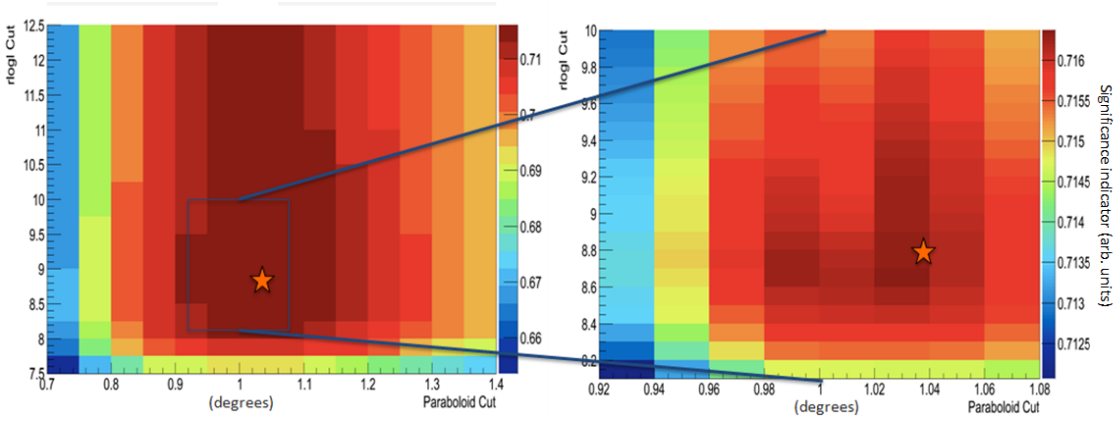

Fig. 4.1: The significance indicator function, Eq. 4.5, is plotted as a function of different cuts on Rlogl and σ_{para}. A cut on the Rlogl parameter (if the cut is larger than 8) do not affect the significance very much. The plot to the right is the blue rectangle in the plot to the left. The star is where we choose to cut, σ_{para}=1.04 and Rlogl = 8.8.

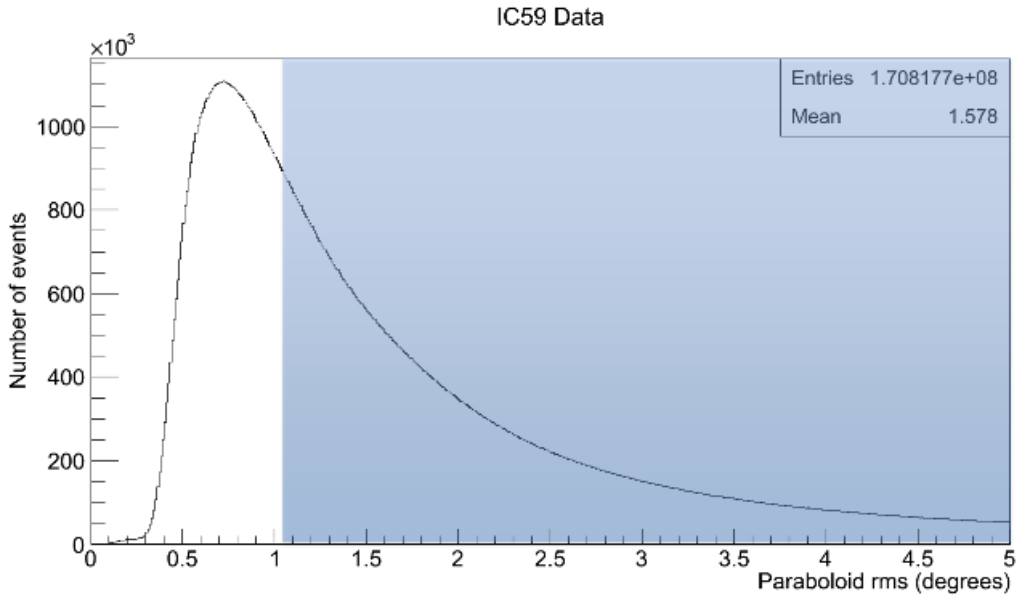

Fig. 4.2: Distribution of the Paraboloid sigma, σ_{par} (called Paraboloid rms in the figure), for the whole data sample. The median of the distribution is 1.3°. All events in the shaded area, with a Paraboloid sigma greater than 1.04 rms, are cut out.

4.1.2 Bin size

The bin size is optimized by using similar arguments as in the previous section.

The square root of the background is proportional to the bin radius:

$$\sqrt{N_{bkgd}} \propto r \tag{4.6}$$

The Point Spread Function (PSF) describes how the events are being spread out. The cumulative PSF (see Fig. 4.10) gives us the fraction of events that are contained within the radius r:

$$N_{sig} \propto \int_0^r PSF \tag{4.7}$$

Using the cumulative point spread function of the sample after quality cuts, we have:

$$S \propto \frac{\int_0^r PSF}{r} \tag{4.8}$$

Maximizing this significance estimator gives an optimal bin radius os 0.79° which is very close to the median angular error, 0.83°.

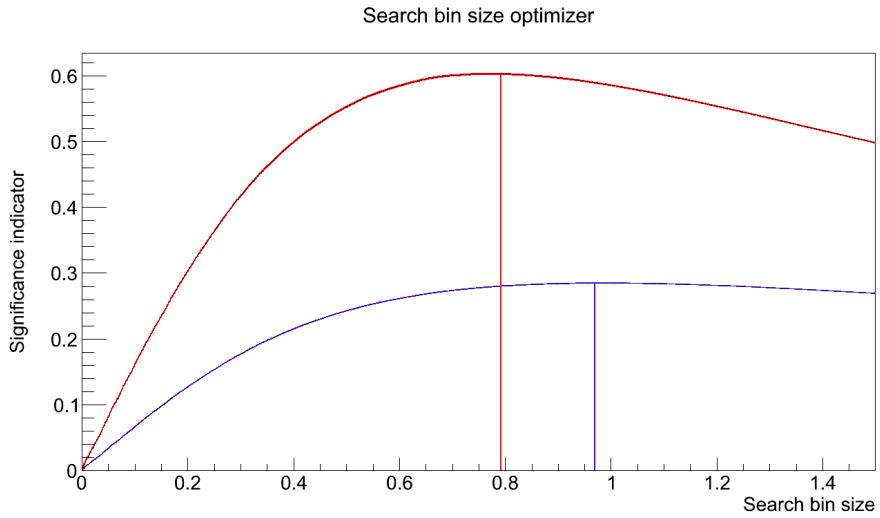

Fig. 4.3: The blue curve is for the simulated data that only has filter level cuts. Since the point spread function is larger without any cuts the optimal bin size is also larger. The red curve has the filter level cuts and the optimized cuts; σ_{par} <1.04 and Rlogl <8.8. The optimal bin size for the sample with optimized cuts is 0.79°.

4.1.3 Results

The standard formula by Li and Ma [10], for calculating the significance of a point source, was used in this analysis:

$$S = \sqrt{2}\left\{ N_{\text{on}} \ln\left[\frac{1+\alpha}{\alpha}\left(\frac{N_{\text{on}}}{N_{\text{on}}+N_{\text{off}}}\right)\right] + N_{\text{off}} \ln\left[(1+\alpha)\left(\frac{N_{\text{off}}}{N_{\text{on}}+N_{\text{off}}}\right)\right]\right\}^{1/2} \quad (4.9)$$

where N_{on} is the number of events in the signal sample, N_{off} is the number of events in the off-source region, and α is the ratio between observing times on- to off-source. We take α instead as the ratio of on- to off-source areas observed, since the times are equal. The above formula was applied to the data using two different binning methods.

Fig. 4.5 shows a radial plot of the count rate as a function of the angular distance from the Moon. The bin around the Moon is a circle with the optimal bin radius 0.79°. The consecutive bins are rings (annulus) with increasing radius, they all cover the same area as the Moon bin. Figure 4.4 illustrate the binning method.

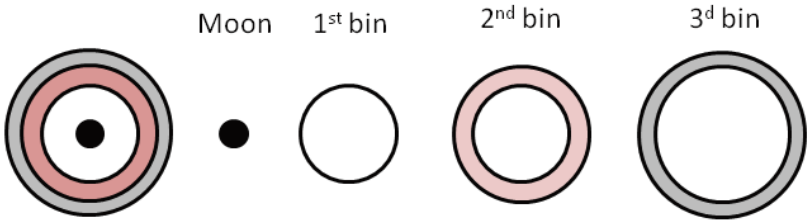

Fig. 4.4: The black circle represent the size of the Moon. The white circle is the circular bin covering the moon. The 2^{nd} bin is a ring surrounding the Moon bin. All the bins in the analysis cover the same area.

The background is calculated by using eight off-source bin configurations to the left and eight to the right of the Moon position. The off-source regions are selected within the same declination band as the on-source region. This is because there is a very strong declination dependence in the down going muon flux, so variations of the order of the Moon deficit are only detectable in right ascension.

The top left plot in Fig. 4.5, is the count rate for the bins centered at the Moon position. With increasing distance from the Moon the count rate in the bins increases, even though they all cover the same area. This is explained by the strong declination dependence in the muon flux. The top right plot is the average count rate for the off-source bins. The

bottom left plot is the top left histogram with the top right histogram subtracted. The neighboring bins to the Moon bin also have a deficit of muons.
The significance: -12 σ for the central bin (the Moon bin) is calculated using Eq. (4.9).

To test the hypothesis that the fluctuations in the background away from the Moon are distributed randomly around 0, we plot them in Fig. 4.6. The width of the Gaussian fit is consistent with 1 (1.2 $\pm$0.2). So the background follows the normal distribution and is therefore consistent with random fluctuations.

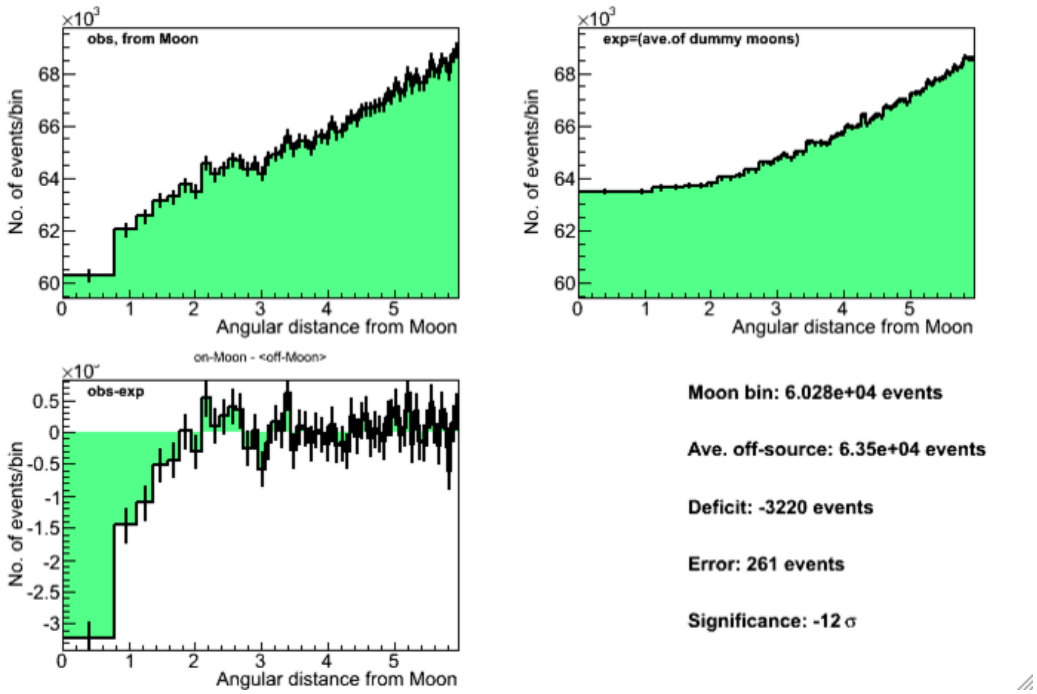

Fig. 4.5: A radialplot of the Moon data sample. The countrate increase with increasing distance from the Moon, this is because the strong declination dependence of the muon flux. There are 3220 events "missing" in the Moon bin. The significance of this deficit is 12 σ, calculated using Eq. (4.9).

The significance map, Fig. 4.8, have been constructed in the following way; The data is first plotted in the standard Moon-centered equatorial coordinates. The plot is binned using 1.4° × 1.4° square bins, covering the same area as the optimized circular bin. Each bin is successively considered as an on-source region. Off-source regions are selected within the same zenith band as the on-source region. Twenty off-source bins are used for each calculation: ten to the right and ten to the left of the on-source region, starting at the third bin out from the on-source bin (i.e. skipping two bins in between, see Fig. 4.7).

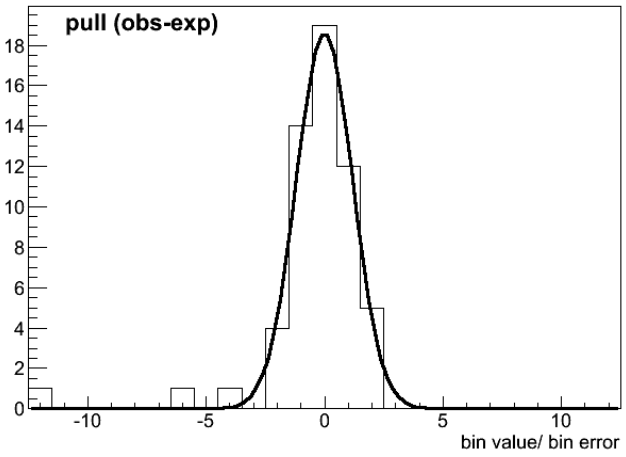

Fig. 4.6: Each deviation in Fig. 4.5 is shown here. A Gaussian is fitted to the histogram, the σ of the Gaussian is 1.2 $\pm$0.2 and it is centered at 0 $\pm$0.2.

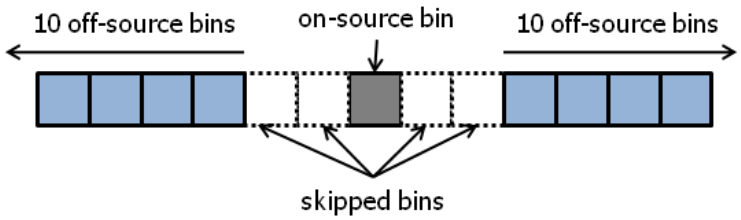

Fig. 4.7: The significance map shown in Fig. 4.8 is calculated in this fashion; The significance of a bin in is calculated by taking 10 off source samples to the left of the on-source bin and 10 to the right, skipping the two closest bins.

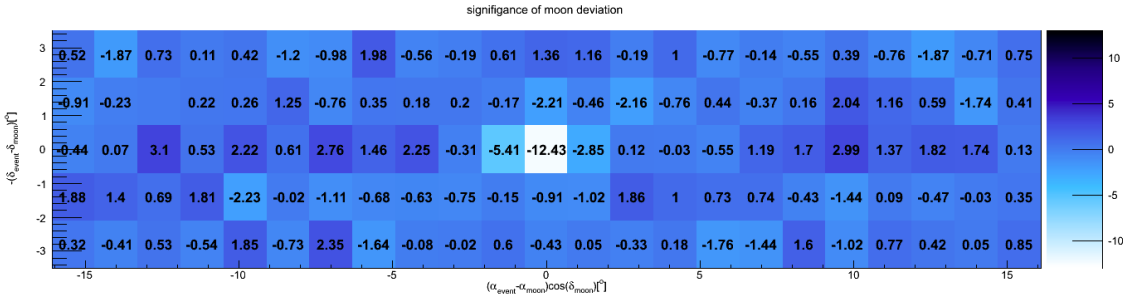

Fig. 4.8: The significance of deviations in a region centered on the Moon. The Moon can be seen as the 12 sigma deficit in the central bin, at (0,0). Fig. 4.7 illustrates the method, Eq. (4.9) is used for the significance calculations.

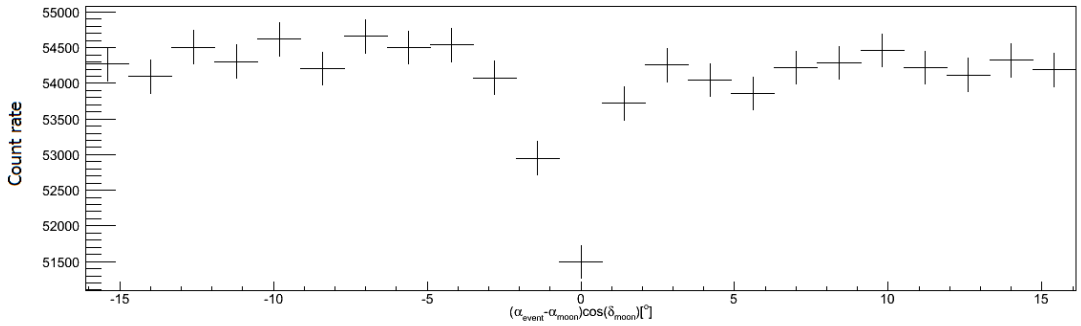

Fig. 4.9: Distribution of the events in a declination band, ±15° from the Moon. The count rate in the bin left off the Moon bin (-1.4°) is noticeable smaller than the bin to the right (+1.4°).

4.1.4 Expected significance

Based on our simulated data set we can estimate what the significance of the deficit should be. The average background for the Moon bin is 63.5k (see Fig. 4.5). The Moon covers 10% of the search-bin's area. Therefore 6.35k events is blocked by the Moon. For a perfect detector we would expect to see this deficit. The resolution of our detector is however not perfect. This results in a blurred image of the Moon shadow. This blurring is described by the point spread function. For a bin with a radius of 0.79°, 48% of the events are contained within that region.

This gives an expected deficit of 3052 ±12 events and a -11.5 σ significance of the deficit, using Eq. 4.9.

We observe a 3220 ±261 events deficit and a -12.2 σ significance of the deficit.

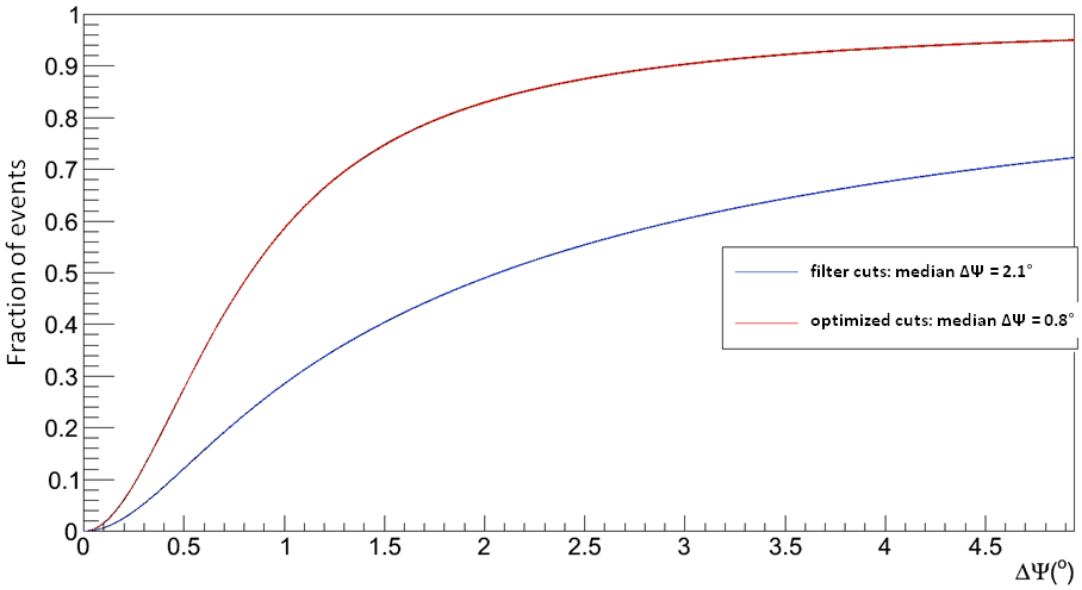

Fig. 4.10: The cumulative point spread function. $\Delta\Psi$ is the angle between the primary cosmic ray and the reconstructed muon track. The median $\Delta\Psi$ means that 50% of the events have an angular difference that is smaller. 48% of the signal from a point source should be seen in a bin with radius 0.79°.

4.2 Fine binned analysis

The fine binned method use smaller bins (0.003 sr) and more of the information available about the events than the previous analysis. The Paraboloid reconstruction gives the uncertainty of the fitted muon track. This information is used in the large binned analysis to cut out events of low quality. In the fine binned analysis this information is used for all the events and only loose cuts are applied to the data.

Each event is described by a probability function, a 2-D Gaussian with a width equal to σ_{par}. These functions are added together into a probability density sky map.

The two-dimensional Gaussian function which describes an event at a given point on the map is:

$$f(x) = A \cdot e^{-\frac{r^2}{2\cdot(\sigma_{par})^2}} \tag{4.10}$$

where A is a normalization factor and r is the angular distance between the event coordinate and the pixel coordinate.

4.2.1 HEALPix

The sky maps in the fine binned method have been constructed using HEALPix (Hierarchical Equal Area isoLatitude Pixelization of a sphere). Healpix is an equal area pixelisation of a sphere. Developed for maps of the CMB (Cosmic Microwave Background).

HEALPix is a binning method suitable for Moon studies since the pixels all cover the same surface area. The pixels are also arranged in bands of constant latitude, this is important because of the strong zenith dependence of the muon flux.

The resolution of the HEALPix grid is expressed by the parameter N_{side}, which defines the number of divisions along the side of a base-resolution pixel. The maps used here have $N_{side} = 1024$ which correspondes to $12 \cdot 10^6$ pixels.

The surface area that one pixel cover is $4\pi/N_{pix}$, where N_{pix} is the number of pixels. This gives in average a resolution of $0.057°$.

4.2.2 Rotation

In the binned analysis the events are centered by subtracting the event's coordinates from the Moon's, $\Delta\alpha = (\alpha_{Event} - \alpha_{Moon}) \cdot cos(\delta_{Moon})$. This creates a small error because one could as well use $cos(\delta_{Event})$ instead of $cos(\delta_{Moon})$. This error is "neglectable" as long as the angular distances are small.

A point on the celestial sphere can be described by a vector. In the fine binned analysis the events are centered by rotating the vector that describes an event's position. The rotation preserves the angular distance between the Moon and the event.

The events are rotated so that they are centered around Right Ascension = 180°, only to simplify some of the calculations because there is a discontinuity at $\alpha = 0$ of the pixel

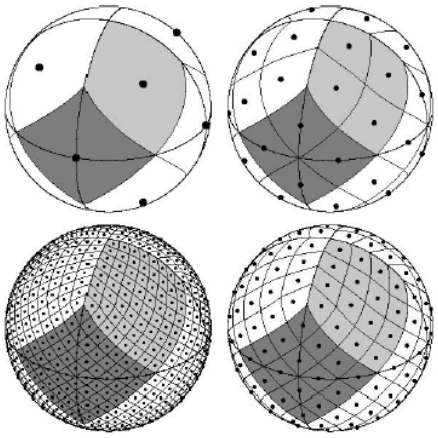

Fig. 4.11: Orthographic view of the HEALPix partition of the sphere. The light grey and the dark grey areas covers the same area. Moving clockwise from the the top left sphere, the grid is subdivided with the resolution parameter equal to $N_{side} = 1$, 2, 4, 8, and the corresponding total number of pixels $N_{pix} = 12$, 48, 192, 768, from [11].

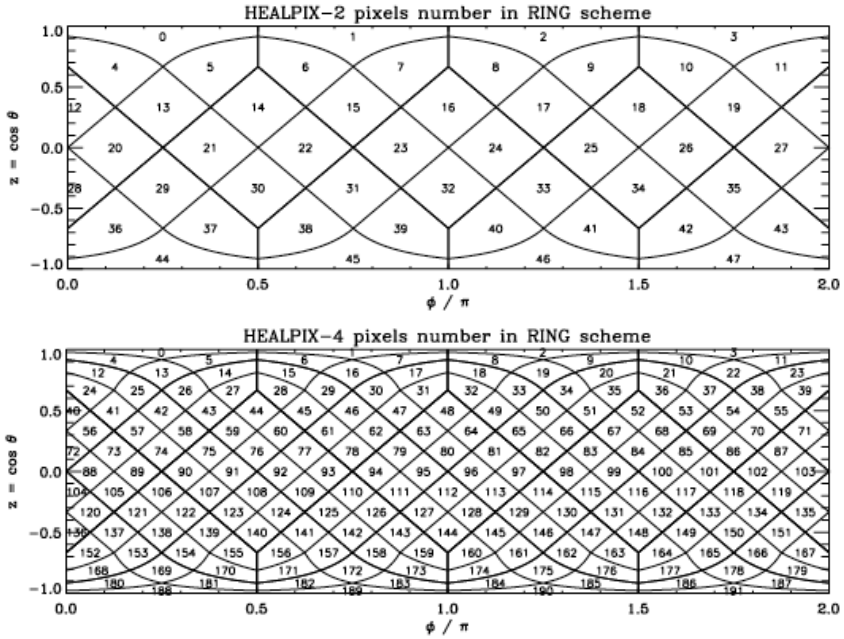

Fig. 4.12: Layout of the HEALPix pixels in a cylindrical projection, the top panel show $N_{side} = 2$ the bottom panel show $N_{side} = 4$. The pixels are numbered in rings of equal latitude.

numbering (see Fig. 4.12), and Declination = the average declination of the Moon (to minimize distortions).

A Point on the healpix sphere is described by the spherical angles (φ, θ). R_y represent a rotation around the y-axis (the z-axis is rotated towards the x-axis):

$$R_y(\varphi) = \begin{bmatrix} \cos\varphi & 0 & \sin\varphi \\ 0 & 1 & 0 \\ -\sin\varphi & 0 & \cos\varphi \end{bmatrix}$$

R_z represent a rotation around z-axis (the x-axis is rotated towards the y-axis):

$$R_z(\theta) = \begin{bmatrix} \cos\theta & -\sin\theta & 0 \\ \sin\theta & \cos\theta & 0 \\ 0 & 0 & 1 \end{bmatrix}$$

The resulting matrix for rotating by θ around the y-axis followed by φ around the z-axis is:

$$R_y(\varphi) \cdot R_z(\theta) = \begin{bmatrix} \cos\theta cos\varphi & -\cos\theta\sin\varphi & \sin\theta \\ \sin\varphi & \cos\varphi & 0 \\ -\sin\theta\cos\varphi & \sin\theta\sin\varphi & \cos\theta \end{bmatrix}$$

A Mollweide equal area projection of a probability density sky map, with a cut on $\sigma_{par} < 2.5^\circ$ can be seen in Fig. 4.13. The cut is used to reduce computation time and events with $\sigma_{par} > 2.5^\circ$ should not contribute much to the deficit. The Moon's position in the map is $(\alpha = 180, \delta = -22)$. Around this positions are events that fall in the filter window ± 40 in α and ± 10 in δ. The strong zenith dependence is the reason for the higher values at the bottom of the window. There is not a clear edge at the edges of the filter window. This is because the reconstructed direction for an event can change after they have gone through the filter at the South Pole because of the more computational heavy reconstructions used at the northern hemisphere.

A band of pixels that all have the same declination, from Fig. 4.13 is shown in Fig. 4.14. At $\alpha = 0^\circ$ the Moon deficit can clearly be seen.

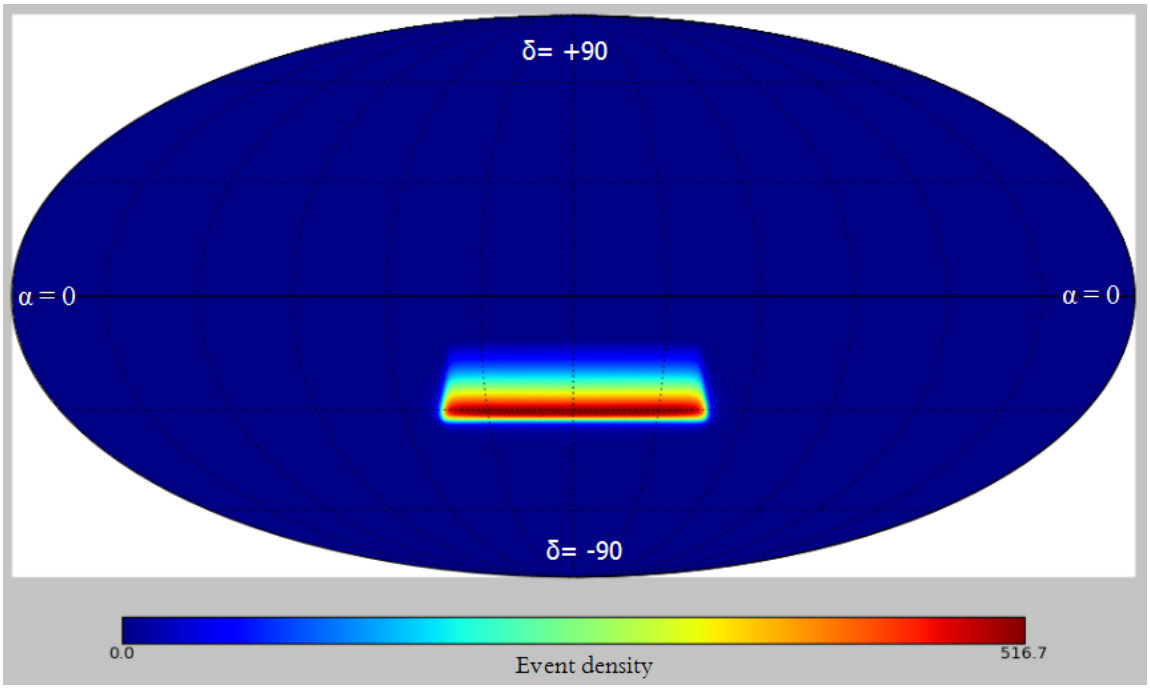

Fig. 4.13: Mollweide equal area projection of the probabilty density sky map. The sphere has 12 million pixels, each pixel covers the same area as a 0.057° square bin (0.003 sr). The events are center around the Moon ($\delta = -22$), and are inside the Moon filter-window (± 40 in α and ± 10 in δ). The declination dependence of the muon flux can clearly be seen.

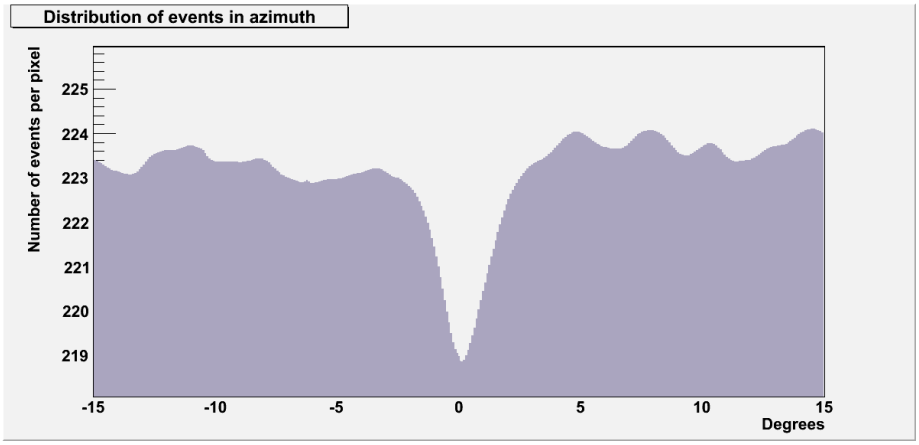

Fig. 4.14: The bins in the histogram corresponds to one pixel in the sky map, Fig. 4.13. The pixels all have the same declination. At $\alpha = 0°$ the Moon deficit can clearly be seen.

4.2.3 Background

From the sky map (Fig. 4.13) a window, ±10° in RA and ±5° in Dec, around the Moon is used to calculate the background. The points on the sky map are now centered at (0, 0) by subtracting the Moon position (180, -22) and multiplying the RA-coordinate with cos(δ) of the point.

A circle with a radius of 2.5° around the moon is ignored when the background is calculated, 2.5° from the Moon the deficit is very small, see Fig. 4.14.

Fig. 4.15 shows part of the window that is taken from the sky map. From these figures one can clearly see that he atmospheric muon flux strongly depends on the zenith angle. This is because the flow of muons gets attenuated by the amount of atmosphere and ice they have to pass.

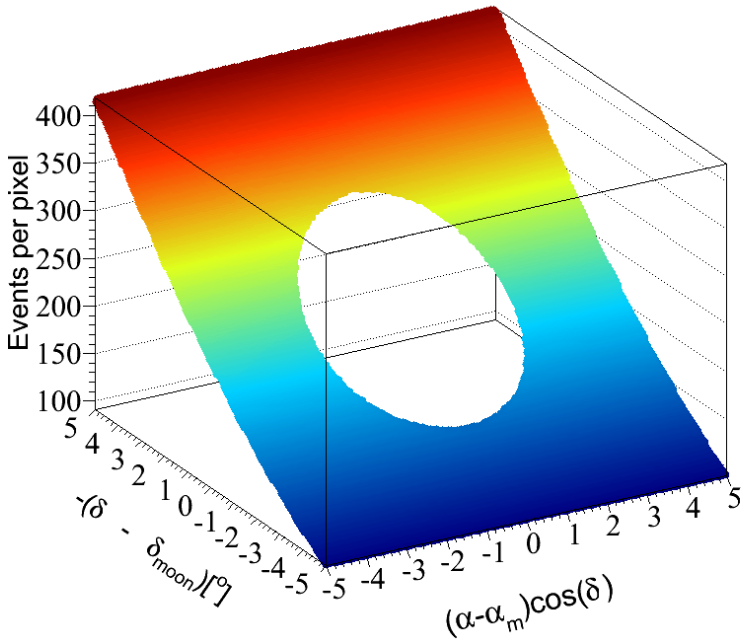

Fig. 4.15: A window is taken from the sky map in Fig. 4.13, ±10° in RA and ±5° in Dec, thus this figure do not show the whole window. The events within a circle of 2.5° around the moon is not used when the background is calculated.

The mean value of the pixels that lay in the same declination band are plotted in Fig. 4.16. The error bars (the variance of the mean) are very small because the pixels are correlated with each other. A 3-degree-polynomial is fitted to the plot.

The fit is then subtracted and the residual is shown in figure in 4.17.

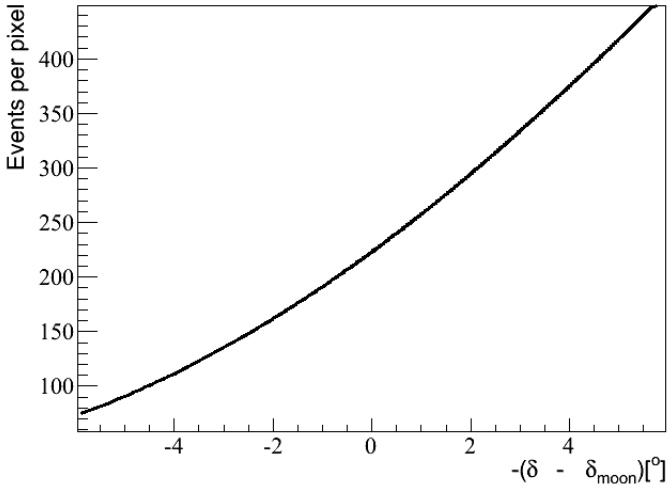

Fig. 4.16: The mean value of each declination band is plotted in this figure with error bars. The error bars are very small because the pixels are correlated. A 3-degree-polynomial is fitted to the background, $\chi^2 = 35$ and NDF=242 but NDF is in realtiy smaller since the points are correlated with each other.

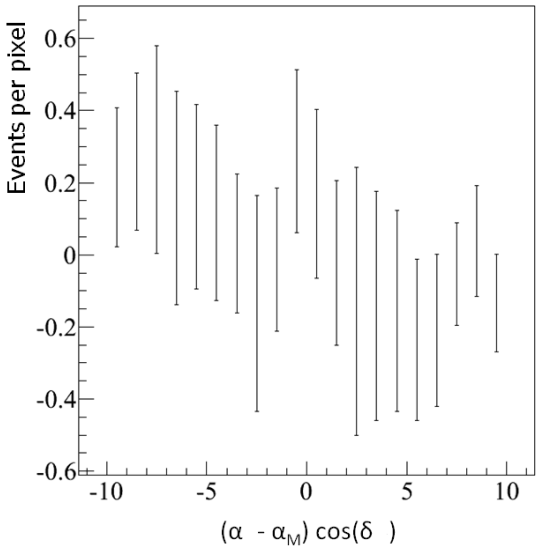

Fig. 4.17: This histogram shows the mean values of the sky map in a side-view after the 3-degree-polynomial in Fig. 4.16 is subtracted. There are some features in the background this comes from the Poissonian behavior of the detection process and from the asymmetry of the detector.

4.2.4 Results

The Moon shadow can clearly be seen after the background has been subtracted. Fig. 4.18 shows the background subtracted map in side-view and Fig. 4.20 shows a top-view of the background subtracted map.

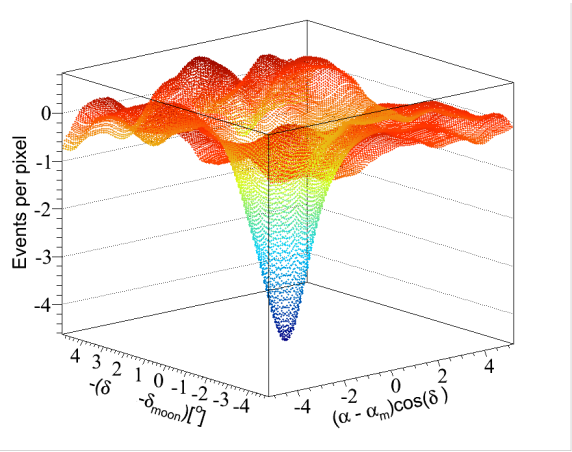

Fig. 4.18: Background subtracted map side-view, the Moon shadow is the sink in the figure.

We fit a Gaussian to the deficit.

$$f(x) = \text{Offset} + \text{Amp} \cdot e^{-\left(\frac{(\alpha-\alpha_{off})^2}{2(\sigma_\alpha)^2} + \frac{(\delta-\delta_{off})^2}{2(\sigma_\delta)^2}\right)} \tag{4.11}$$

The parameters of the Gaussian function is shown in Fig. 4.19, and Table 4.1 shows the results off the Gaussian fit to the deficit.

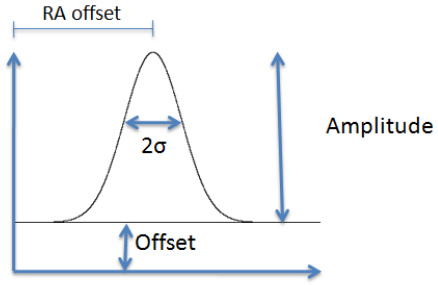

Fig. 4.19: A 2D-Gaussian is fitted to the deficit.

The median PSF, Ψ_{med}, is 1.4° for a cut on $\sigma_{par} < 2.5°$. This is greater than the width of the Gaussian that is fitted to the deficit, see Table 4.1, but this is not too surprising since the events with a smaller Ψ, in average, gets a larger weight.

Table 4.1: A Gaussian is fitted to the deficit, Eq. 4.11, the parameters are explained in Fig. 4.19. The uncertainties are the uncertainties from the fit, no errors from the Poissonian behavior of the detection process is considered.

Parameter	Value	Uncertainty of the fit
Amplitude	-4.21	0.05
Offset	0.023	0.004
α_{offset}	-0.10°	0.01°
δ_{offset}	0.02°	0.01°
σ_α	1.09°	0.01°
σ_δ	0.89°	0.01°

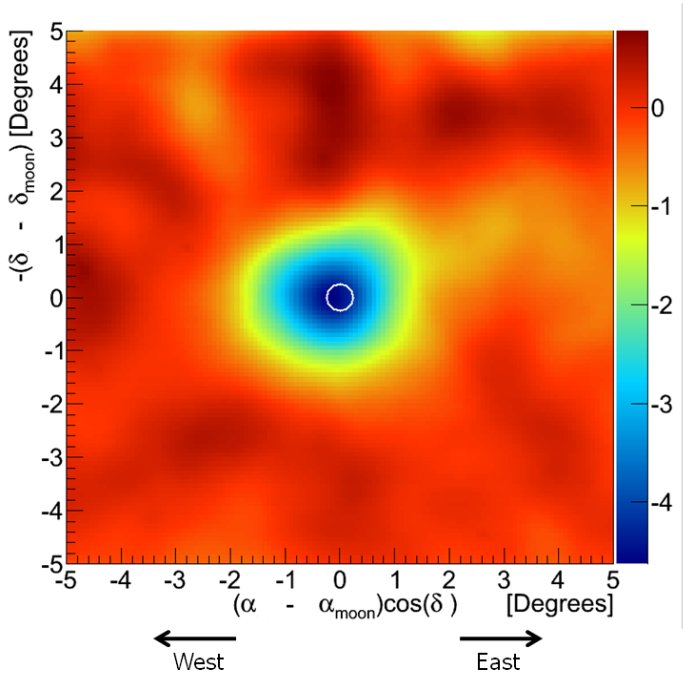

Fig. 4.20: Background subtracted map top-view, the white circle with a radius of 0.25° represents the Moon. The shadow is shifted and looks more "smeared out" in the West-ward direction. Earth's magnetic field should cause a small shift of the Moon shadow in the West-ward direction and also affect the width of the shadow in this directions, see Fig. 2.10.

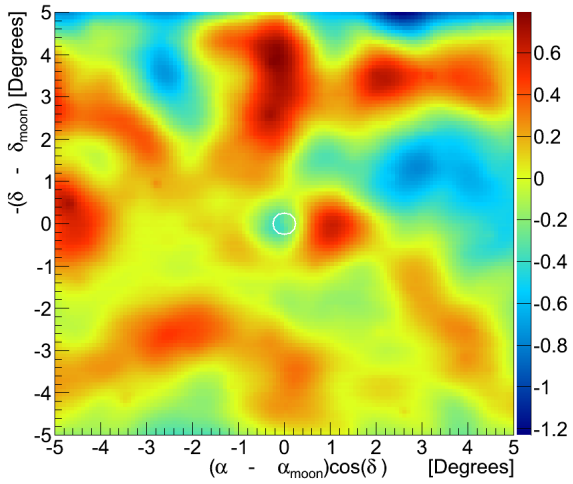

Fig. 4.21: Residual plot with the fitted Gaussian subtracted.

To test if the shift depends on the energy of the primary cosmic ray we divide the data sample by the median reconstructed energy (using the MuE energy reconstruction) into two equal parts. Fig. 4.22 shows a top-view of the low energy sample and Fig. 4.23 the high energy sample. These plots have a cut on $\sigma_{par} < 1°$.

A Gaussian is fitted to the two shadows. The results are given in Table 4.2.

We also divide the simulated data into two parts by the median reconstructed energy of the simulated events. The two distributions of the primary energy is plotted in Fig. 4.24. The deflection angle for the median low energy and high energy sample is 0.07° and 0.03° respectively, calculated with Eq. 2.12.

It is difficult to draw any conclusions from these figures. The fit to the high energy shadow is shifted more than the fit to the low energy shadow but the low energy Gaussian is also wider. However, this suggest that the shift is not due to the geomagnetic field.

Table 4.2: The data is divided by the median energy into a low energy data sample and a high energy data sample. A Gaussian is fitted to the two deficits, in Fig. 4.22 - 4.23. The uncertainties are only the uncertainties from the fit itself.

	Low energy		High energy	
Parameter	Value	Uncertainty	Value	Uncertainty
Amplitude	-1.91	0.05	-2.09	0.06
α_{offset}	-0.14°	0.03°	-0.19°	0.02°
δ_{offset}	0.06°	0.02°	-0.03°	0.02°
σ_α	1.03°	0.03°	0.86°	0.02°
σ_δ	0.83°	0.02°	0.83°	0.02°

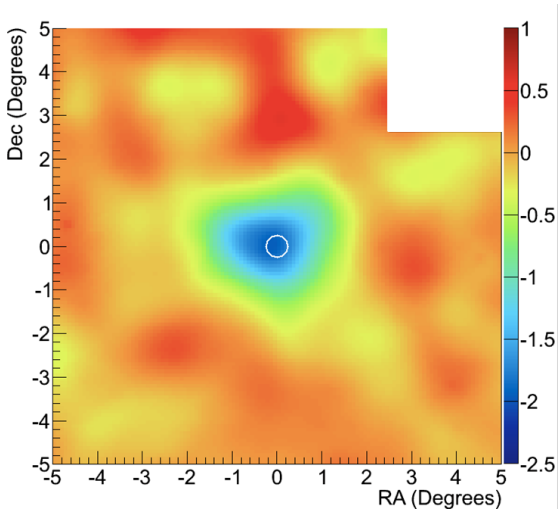

Fig. 4.22: Top-view of the Moon shadow of the low energy sample.

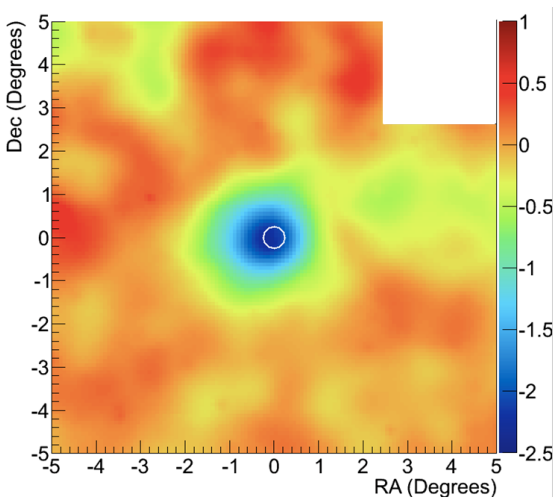

Fig. 4.23: Top-view of the Moon shadow of the high energy sample.

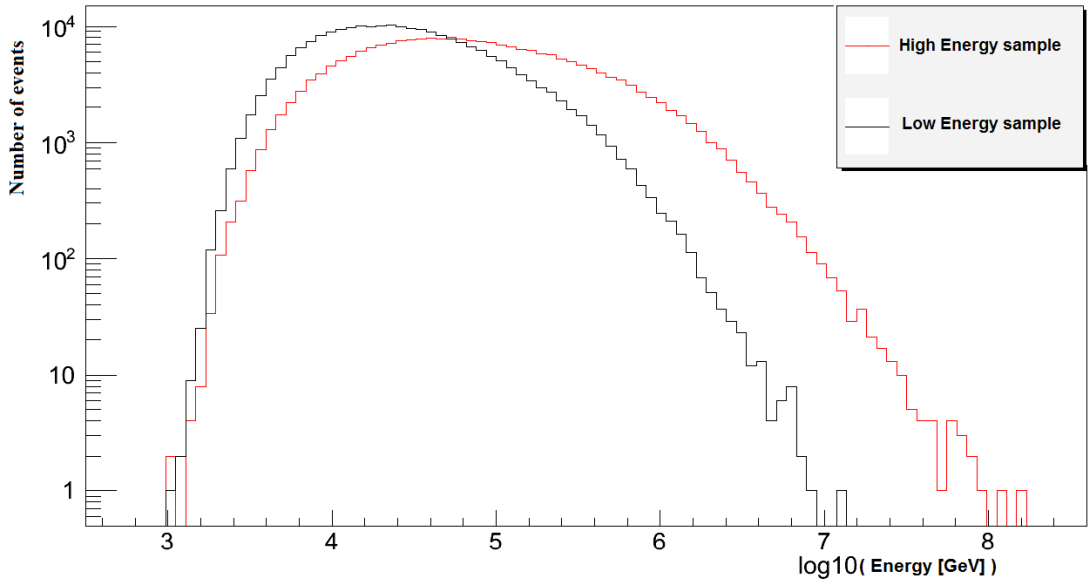

Fig. 4.24: Energy distribution of simulated data divided into a high and low energy sample. The black curve is the high energy sample and the red the low energy sample.

Chapter 5

Conclusions and outlook

The 59-string configuration of IceCube observe the Moon shadow at the 12σ confidence level and our understanding of the angular resolution of the detector is in agreement with the results of the analysis. This is an important result because it shows that there are no serious problems with the detector.

The position of the Moon shadow can be used to test the pointing accuracy. The shift in the position of the Moon discovered in this work is small, much smaller than the PSF. However it is important to know if there is a systematic pointing error, especially when looking for sources in the sky. Therefore it would be worthwhile to develop the method used here to better estimate uncertainties in the shift of the shadow. Simulations indicate that the median energy of the detected cosmic rays from the direction of the Moon is 38 TeV. The resulting magnetic deflection at these energies is very small. It is difficult to believe that the magnetic field is solely responsible for the shift but it cannot be ruled out at this stage. It should be pointed out that the observed shift could be within the uncertainties of the method.

One way to improve the fine binned analysis would be to use the "time-scrambling" technique when calculating the background. In this method the detection times of the events are scrambled, this results in new RA coordinates for the events. This method naturally takes into account any systematic biases when estimating the background, except for time-dependent biases.

The next Moon shadow analysis will use data from the 79-string version of the detector. This version has taken data since June 2010. If a small shift is seen in this version then we need to investigate what could cause such a shift.

Bibliography

[1] *Victor F. Hess - Nobel Lecture*, Nobelprize.org, http : //nobelprize.org/nobel_prizes/physics/laureates/1936/hess − lecture.htm Dec 2010

[2] C. Amsler et al. *Particle Data Group*, Physics Letters B667, Issues 1-5 (2008)

[3] L. Bergström, and A. Goobar, *Cosmology and Particle Astrophysics* 2:nd Edition, Springer-Verlag 2004

[4] D. Chirkin, W. Rhode, *Propagating leptons through matter with Muon Monte Carlo (MMC)*, arXiv:hep-ph/0407075v2 Feb 2008

[5] T. Stanev, *High Energy Cosmic Rays* 2nd edition, Springer-Verlag 2010

[6] G.W. Clark, *Arrival Directions of Cosmic-Ray Air Showers from the Northern Sky*, Physical Review Vol 108, no 2, October 1957

[7] Till Neunhffer, *Estimating the angular resolution of tracks in neutrino telescopes based on a likelihood analysis*, arXiv:astro-ph/0403367v1 Mar 2004

[8] G. Di Sciascio a and R. Iuppa *Measurement of the $\bar{p}/p$ ratio in the few-TeV energy range with ARGO-YBJ*, arXiv:1011.2637v1 [astro-ph.HE] Nov 2010

[9] M. Amenomori, et a *Multi-Tev Gamma-Ray Observation from the Crab Nebula Using the Tibet-III Air Shower Array Finely Tuned by the Cosmic-Ray Moon's Shadow*, arXiv:0810.3757v1 [astro-ph] Oct 2008

[10] Li, T.-P. and Ma, Y.Q., *Analysis methods for results in gamma-ray astronomy* 1983, ApJ 272,317

[11] Gòrski et al., *HEALPix: A Framework for High-Resolution Discretization and Fast Analysis of Data Distributed on the Sphere* The Astrophysical Journal, 622:759771, April 2005

[12] Francis Halzen, Spencer R. Klein, *IceCube: An Instrument for Neutrino Astronomy*, arXiv:1007.1247v2 [astro-ph.HE] Aug 2010

[13] Morgan Wascko, "Study of the Shadow of the Moon in Very High Energy Cosmic Rays with the Milagrito Water Cherenkov Detector", PhD thesis, March 2001